Compton Weighting Schemes for a Liquid Xenon PET System

by

Matthew Curtis Gottschalk

A THESIS SUBMITTED IN PARTIAL FULFILLMENT OF
THE REQUIREMENTS FOR THE DEGREE OF

BACHELOR OF SCIENCE

in

The Faculty of Science

(Honours Physics)

THE UNIVERSITY OF BRITISH COLUMBIA

(Vancouver)

April 2012

Abstract

A novel liquid xenon positron emission tomography (LXePET) system currently under development at TRIUMF will push PET imaging to its ultimate capability. By accompanying this high resolution PET detector, Compton weighting schemes have the potential to improve the quality of reconstructed images. A simulation of the LXePET detector using the National Electrical Manufacturers Association mouse and rat phantoms has been used to characterize the performance of various weighting schemes. The weighting schemes investigated were performed externally and internally to maximum likelihood expectation maximization image reconstruction routines.

Table of Contents

Abstract ii

Table of Contents iii

List of Tables v

List of Figures vi

Acknowledgements viii

Dedication ix

1 Introduction 1

2 Theory 10

2.1 Compton Reconstruction 10

2.2 MLEM 15

3 Experimental Methods 17

3.1 Geant4 Simulation 17

3.2 Image Reconstruction 19

3.3 Analysis Tools 20

3.3.1 Phantoms 20

3.3.2 Scatter Fraction Calculation 20

3.3.3 Image Resolution 21

4 Results and Discussion 24

4.1 Inverse χ^2 Weighting 25

4.2 Internal MLEM Weighting 30

5 Conclusion 41

Bibliography 43

List of Tables

1.1 Comparison of different commercially used scintillators. 4

2.1 Identifier definition for each topology 11

3.1 FWHM and FWTM for the mouse and rat phantoms. 22

4.1 Properties of reconstructed images for the mouse and rat phantoms . 26

4.2 Properties of the mouse and rat phantom images reconstructed for each topology. 34

4.3 Properties of the mouse and rat phantom images reconstructed with the internal MLEM weighting scheme. 35

List of Figures

1.1 Basics of medical PET. 2
1.2 Possible event scenarios in a PET detector. 3
1.3 Schematic of the LXePET detector. 6
1.4 Operating principles of a LXeTPC. 7
1.5 Example 1D profile of a reconstructed mouse phantom accompanied with the source distribution profile. 9

2.1 Probability that an event has a certain topology. 12
2.2 Probability that the Compton reconstruction algorithm identifies the correct LOR for each topology. 12
2.3 Probability that the Compton reconstruction algorithm identifies the correct LOR as a function of scatter angle. 13
2.4 Probability that the correct LOR is contained in the ten most likely interaction sequences. 13

3.1 Axial view of the simulated detector geometry. 18
3.2 List mode MLEM reconstructed images for the mouse and rat phantoms. 19
3.3 1D profile for the mouse phantom showing FWHM and FWTM. . 23

4.1 External and internal weighting schemes. 25
4.2 MLEM reconstructed images of the mouse phantom with inverse χ^2 weighting. 27

4.3 MLEM reconstructed images of the rat phantom with inverse χ^2 weighting. 28
4.4 Profiles of the mouse and rat phantoms with inverse χ^2 weighting. 29
4.5 MLEM reconstructed images of the mouse phantom for topologies 1–1 to 1–3. 31
4.6 MLEM reconstructed images of the rat phantom for topologies 1–1 to 1–3. 32
4.7 Profiles of the mouse and rat phantoms for each topology. 33
4.8 MLEM reconstructed images of the mouse phantom with the internal weighting scheme. 36
4.9 MLEM reconstructed images of the rat phantom with the internal weighting scheme. 37
4.10 Profiles of the mouse and rat phantoms for the internal weighting scheme. 38
4.11 MLEM reconstructed images of the mouse and rat phantoms for an external weighting scheme. 39

Acknowledgements

I would like to express my gratitude towards all those who made this thesis possible. To my supervisor Doug Bryman for introducing me to the field of high performance medical imaging instruments and facilitating this project. To Alice Miceli for her continual support and direction when encountering obstacles. Finally, to the rest of the LXePET team at TRIUMF and the TRIUMF administration.

Dedication

For my family.

Chapter 1

Introduction

Non–invasive medical imaging techniques provide the medical community with a unique perspective into the human body while offering a decreased risk to the patient. Positron emission tomography (PET) is one of these techniques. PET images the function of a patient's organs, which is different from other medical imaging modalities such as MRI or X-ray that image soft and hard tissue. PET is an invaluable tool in the diagnosis of several diseases, including cancer, cardiac and neuropsychiatric diseases [10]. Current preclinical PET scanners in use have a spatial resolution of about 2 mm. A group at TRIUMF led by Dr. Doug Bryman is developing a liquid xenon (LXe) based PET system to improve PET imaging to its ultimate capability.

In PET, a patient is injected with a tracer containing positron–emitting nuclides [9]. A diagram showing the basic PET principles is shown in Figure 1.1. The tracer is attached to a biologically active molecule chosen to target a specific bodily function. For example, fluorodeoxyglucose (FDG) is predominantly used in clinical oncology as it is an analog to glucose. After being taken up in the cells it is trapped until it decays [2]. Through β^+ decay the radionuclides emit a positron into the surrounding tissue. The positron slows down and then annihilates with a nearby electron. The annihilation typically occurs within a distance of a few millimeters from the decay site and produces two photons. The positron and electron are nearly at rest before annihilation. Momentum and energy conservation require that these photons are emitted close to 180° with each having an energy near 511 keV. By detecting both photons and determining their detection coordinates a line of response (LOR) between their positions can be

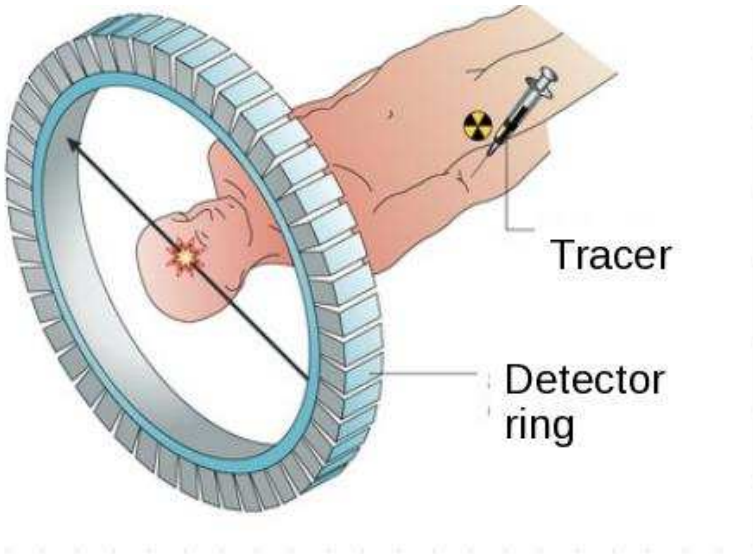

Figure 1.1: Medical PET imaging. A patient is injected with a radiotracer. The radiotracer goes throughout the body and decays resulting in the production of two photons. The photons are detected in coincidence by a ring of detectors. The line of response passing through the decay site is used to reconstruct a map of radioactivity.

assigned. The information combined from many LORs allows the distribution of the radionuclide to be reconstructed. A region with higher radioactivity will have more LORs passing through it, as compared to lower radioactivity regions, and will be given a higher intensity in the reconstructed image.

The goal of a PET system is to detect photons from the same annihilation event and reconstruct the true LOR. A photon can scatter with electrons on the way to the detectors. This interaction decreases the energy of the photon and alters its direction (the most likely interaction is Compton scattering and is discussed in § 2.1). If either photon scatters on the way to detection a false LOR can be assigned and distortions will be produced in the reconstructed image. To limit the amount of scatter events introduced into the image only photons with energy around 511 keV are accepted. A PET system with high energy resolution

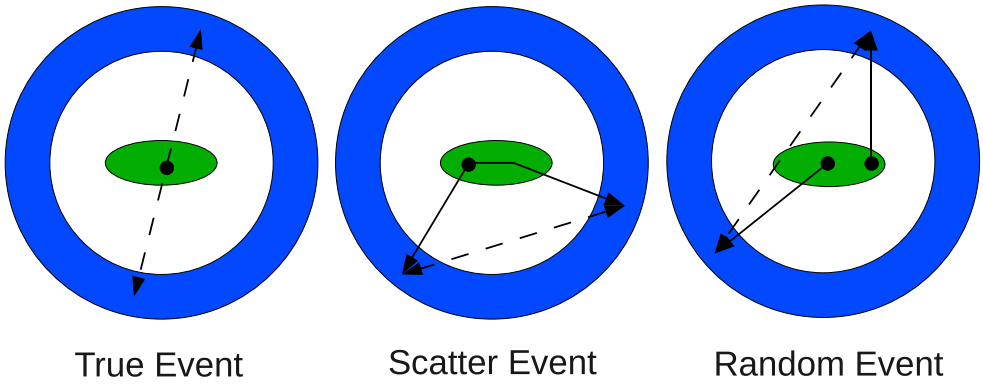

Figure 1.2: The three different scenarios leading to a LOR being assigned. The dashed lines indicate LORs, while the solid lines indicate photon paths. The LORs assigned for scatter and random events can lead to distortions in the image. A detector with higher energy resolution and a shorter coincedence window will perform better by removing scatter and random events.

will be able to separate out the photons with decreased energy due to scattering from the unscattered photons near 511 keV.

Another process affecting the quality of PET images is the chance that two photons from different annihilation events can be assigned to the same LOR. A time window between photon detections is enforced to prevent random coincidence events. By shortening the coincidence time window the number of random events will be reduced. The different types of events that can be assigned LORs is shown in Figure 1.2.

Conventional PET systems typically use crystal scintillators and photomultiplier tubes (PMTs) for detecting photons. Their designs range from circular detector rings to detectors mounted on a rotating gantry. Their ability to determine different detection points is limited by the size and arrangement of the scintillators. Furthermore, their energy resolution is related to the type of scintillator material. The performance of current PET systems is highly dependent on the choice of scintillator. A faster operating scintillator will allow a shorter

Scintillator	NaI	BGO	GSO	LXe
Effective Atomic Number	50	73	58	54
Density	3.7	7.1	6.7	3.0
Relative Light Output (%)	100	15	20–40	80
Energy Resolution (%)	-	15	25	<10
Spatial Resolution (mm)	-	4.8	4.8	<1.0
Decay Time (ns)	230	300	60	2.2,27,45

Table 1.1: A comparison of the different types of scintillator used in various PET systems. The energy resolution and spatial resolution of BGO and GSO are given for systems that are commercially available [3]. The values for LXe are obtained from simulation [11]. The light output for LXe is for zero applied electric field. LXe shows a significant advantage over the commercially available systems.

coincidence window reducing the number of random events, while a scintillator with higher energy resolution will be able to reject more scatter events.

A crystal scintillator detector (typical arrangement is shown in Figure 1.1) is limited by the size of it's crystals. Smaller crystal size produces higher resolution images as the radioactivity can be located to smaller regions. As the crystals become smaller the energy resolution of the scintillator worsens. Crystals also suffer from parallax error as there is generally no information about the depth of the interaction. Parallax error can produce uncertainties in the correct interaction points as large as the crystal size. Events spanning multiple crystals provide another problem for crystal scintillator systems. Events going through multiple crystals must be rejected as it can be unclear which scintillator is triggered first.

The LXePET system under development uses ionization and scintillation light signals from photon interactions in LXe. LXe can be easily arranged in large, homogeneous volumes providing high uniformity over the entire field of view. The high atomic number (54) and high density (3.0 g cm^{-3}) make it efficient at stop-

ping radiation and a good material for detecting photons [4]. A comparison of different scintillators is shown in Table 1.1. Aside from scintillation, electron–ion pairs are also produced when energy from radiation is deposited in LXe. The number of pairs produced is proportional to the energy deposited, therefore by collecting the electrons and scintillation photons the energy deposited can be reconstructed. If an electric field is applied to LXe the electrons drift through the material with a constant speed [5]. By combining the information from the scintillation signal and the ionization signal the energy and position of the incoming annihilation photon can be determined. Using the combined energy information LXe has a higher energy resolution and shorter decay times than currently used scintillators [3].

A diagram of the LXePET scanner being developed is shown in Figure 1.3. The detector is composed of multiple LXe time projection chambers (TPCs) arranged in a ring. The scintillation light is measured by large area avalanche photodiodes (LAAPDs) on the side of each TPC. An electric field is applied axially to drift electrons away from the center of the detector. The anode consists of a shielding grid, a layer of wires and a set of anode strips oriented at 90° to the wires as shown in Figure 1.4. As the electrons drift past the shielding grid they induce a signal in the wires. The electrons get collected by the anode strips. Measuring the signal from the wires and the strips gives the x–y position of the interaction. This is the x–y position in the frame of each TPC. The scintillation light gives the initial time of ionization and the signal measured by the wires and strips gives the drift time. Using simple kinematics the z position can be found by knowing the drift velocity for an applied electric field.

The position resolution of the proposed PET system is sub–mm, smaller than any crystal scintillator currently used for PET. The high 3D position resolution in LXe removes the parallax error as the depth of the interaction is measured. Reconstructing the path of the photon also gives LXe an advantage over crystal scintillators as events that would have spanned multiple crystals can be included.

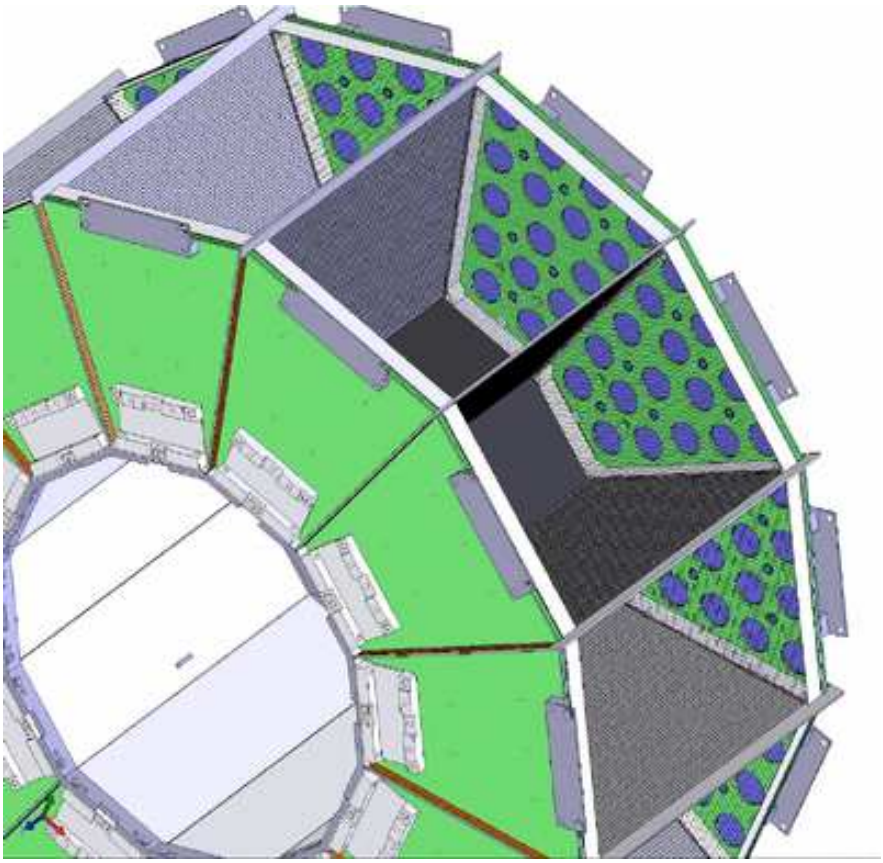

Figure 1.3: A diagram showing the LXePET system being developed. The detector is composed of 12 trapezoidal sectors arranged in a ring geometry. The entire ring is contained in a stainless–steel vessel thermally insulated by a vacuum space. The vessel is filled with LXe for producing scintillation and ionization signals. Each sector is a time projection chamber for determining the 3D position of the photon interaction points. The inner bore of the detector is 10 mm in diameter and is suitable for studying small animals such as mice or rats.

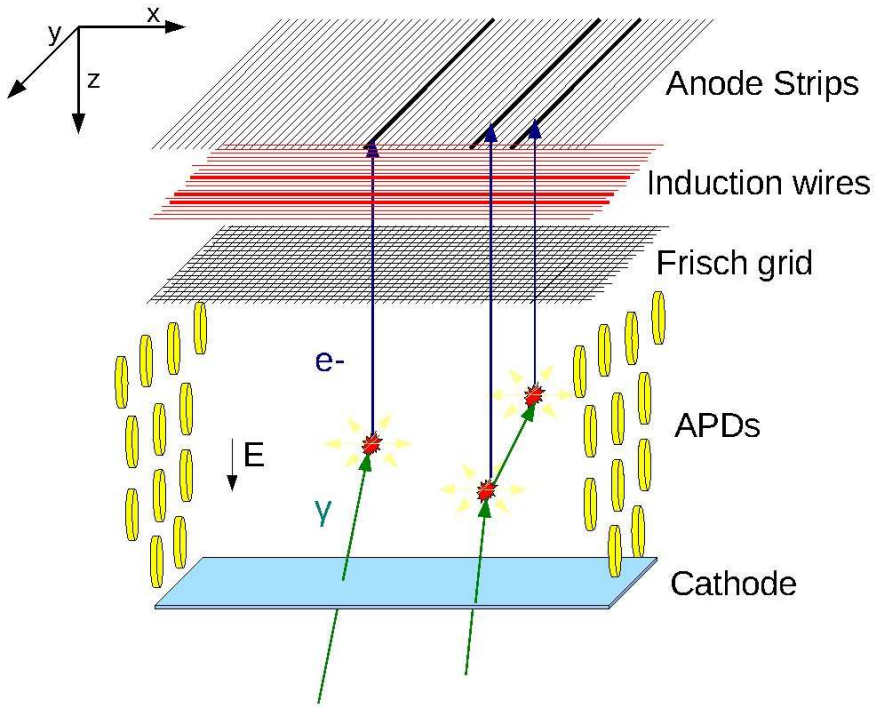

Figure 1.4: A representation of the operating principles for one TPC. A photon enters the chamber and produces scintillation light and ionization. The APDs view the scintillation signal. The electrons drift from the cathode to the anode where they are measured on the wires and strips. The x–y position is determined from the wires and strips that register a signal. The difference in time between the scintillation signal and the anode signal allows the z position to be determined. This is done by assuming a constant drift velocity for an applied electric field.

An incoming photon from annihilation can Compton scatter within each module multiple times before being photo–absorbed. At 511 keV a photon has a higher probability of being scattered than being absorbed. Multiple scattering deposits the energy at multiple interaction points. The energy and position at each scattering position must be used to determine the first interaction point and to develop the correct LOR. A Compton reconstruction algorithm uses the information from each interaction point and goes through each possible interaction sequence. The algorithm assigns each sequence a statistical weight, called the χ^2. The interaction sequence with the lowest χ^2 is chosen and it's associated LOR is recorded for image reconstruction. The χ^2 information is used no further. There is a non–zero probability that the LOR taken will not be the true LOR. This is similar to taking a scattered or random LOR.

A profile from a cylindrical source of radius 1.6 mm is shown in Figure 1.5. There is a significant amount of signal further than 1.6 mm from the center of the source. This signal is a result of the Compton reconstruction inefficiency in determining the correct LOR. The probability that the LOR is the correct one is related to it's χ^2 value. If this information is used further in the image reconstruction higher quality images could be produced. A group of methods which have been proposed to improve image quality for a LXePET detector are the Compton weighting schemes [7]. These schemes use the χ^2 values to give more weight to the more likely LORs. Weighting attempts to reduce the ambiguities of the Compton reconstruction algorithm. This study looks at various Compton weighting schemes and their performance as pertaining to a LXePET detector. The Compton reconstruction algorithm and the image reconstruction is discussed in § 2. The data and analysis tools are outlined in §3. The Compton weighting schemes are tested and their behaviour are analyzed in § 4.

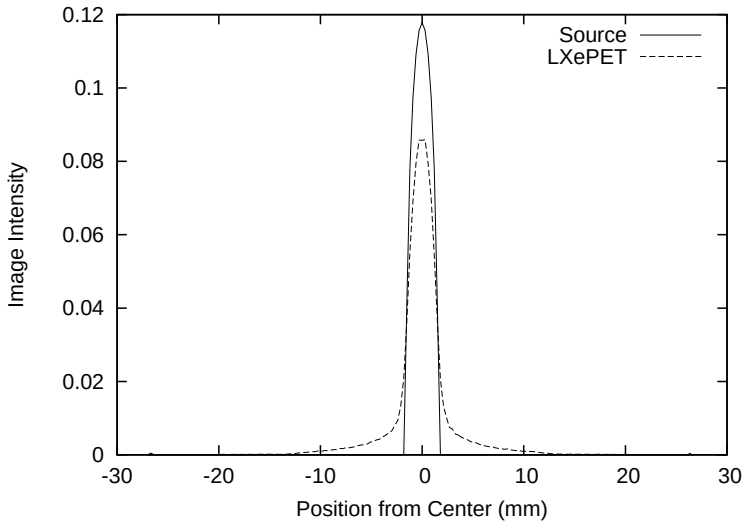

Figure 1.5: Simulated line profiles from a 1.6 mm radius ^{18}F cylindrical source. The solid line shows the source distribution. The dashed line shows the simulated response of a LXePET detector. The nature of PET and the response of the detector causes signal farther than 1.6 mm from the center of the source. The signal outside of this region is the result of scattered LORs being included in the image, positron range before annihilation and the photon non–collinearity.

Chapter 2

Theory

The basic theory for determining the correct LOR is outlined in § 2.1, as well as a brief definition of topology types. The theory behind the image reconstruction method is outlined in § 2.2. The implementation and use of the MLEM method, as it pertains to this study, is further described in § 3.2.

2.1 Compton Reconstruction

A photon interacting in liquid Xe is either photo–absorbed or scattered. The predominant mode of interaction is Compton scattering. A 511 keV photon is nearly three times more likely to scatter. A photon can scatter multiple times in LXe before being completely photo–absorbed. These Compton scattering interactions produce scintillation light and ionization charges, which the TPCs use to reconstruct the interaction positions in 3D and the energy deposited in the detector. The number of interaction points in each contributing TPC determines the complexity of the interaction sequence, called the topology of the event. Each topology considered can be mapped to a number on $[0 : 9]$. The topology definitions are listed in Table 2.1. The simplest interaction configuration is the 1–1 topology (one interaction in each TPC). More complex sequences, such as 1–2 (one interaction in one TPC and two interactions in the other), 2–2 and 2-3 and 1–3 contribute a significant amount to the total number of events. The proportion of events for each topology is shown in Figure 2.1. The 1–2 topology is the most likely event.

The location of the first interaction points must be determined to assign the

Topology	Identifier	Topology	Identifier
1–1	0	3–3	5
1–2	1	1–4	6
2–2	2	2–4	7
1–3	3	3–4	8
2–3	4	1–5	9

Table 2.1: The identifier for a particular topology. This labeling is used for Figures 2.1, 2.2, 2.4.

correct LOR. For the 1–1 topology there is only one possible LOR to assign, but for more complex topologies many different LORs could be assigned. This produces an ambiguity in the location of the first interaction point and contributes to blurring of the image. The timing of the events is not sufficient to determine the first interaction point.

To find the correct first interaction points a Compton reconstruction algorithm [6] is used. For an M–N topology there are $M!N!$ different interaction sequences. This algorithm sorts through all possible interaction sequences to determine the most probable path of the photon through the detector. When a photon Compton scatters in liquid Xe the scatter angle, θ_E, as function of the incoming and outgoing photon energies is given by

$$\cos\theta_E = 1 + mc^2 \times (E_i^{-1} - E_f^{-1}) \tag{2.1}$$

where E_i is the energy of the photon before scattering, E_f is the energy of the photon after scattering and m is the mass of the electron. Furthermore, the angle, θ_G, of the scattered photon can be determined geometrically from the positions of three consecutive interaction points

$$\cos\theta_G = \frac{\vec{u_i} \cdot \vec{u_f}}{|\vec{u_i}||\vec{u_f}|} \tag{2.2}$$

where $\vec{u_i}$ is the direction from the first to the second interaction point, and $\vec{u_f}$ is the direction from the second to the third interaction point. By calculating θ_G and

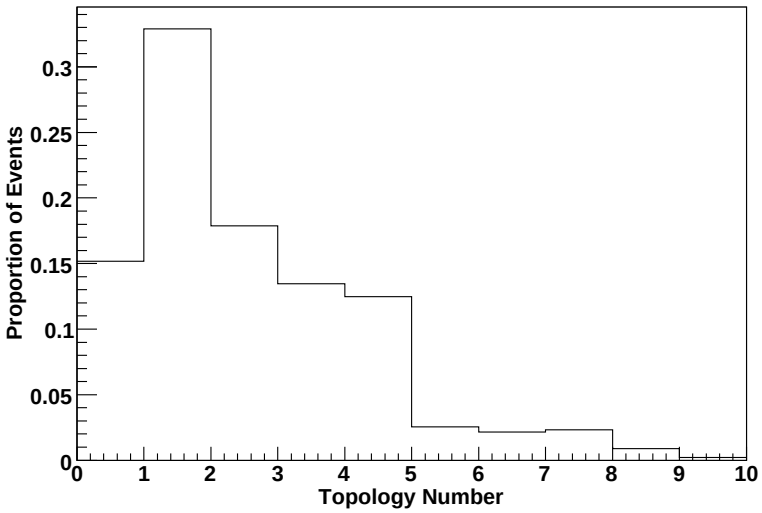

Figure 2.1: The probability that a given event will have a certain topology. The most likely topology is 1–2 followed by 2–2 and 1–1. Toplogies higher than 1–3 contribute around 10% combined to the total number of events.

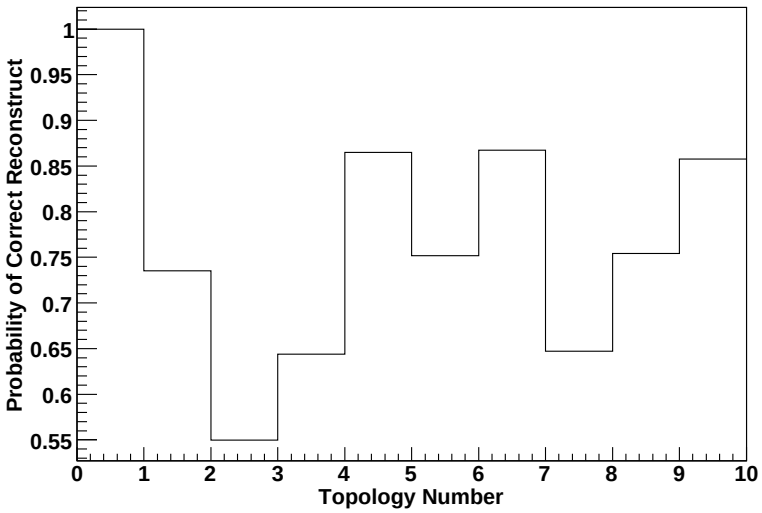

Figure 2.2: The ability of the Compton reconstruction algorithm to find the correct LOR for each topology. The poor performance for the 1–2, 2–2 and 2–3 topologies is due to the ambiguity in the interaction sequence for events with two events in one TPC. At higher topologies the algorithm performs better, but these events contribute very little to the total number of events.

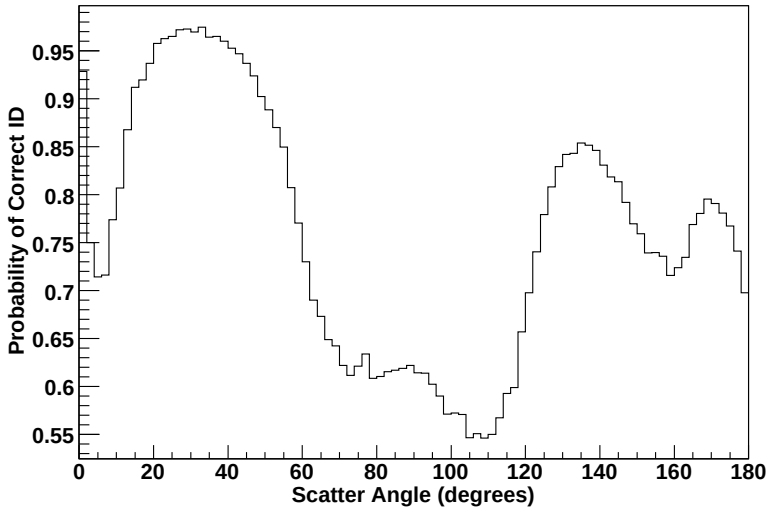

Figure 2.3: Probability the correct sequence is found from the Compton reconstruction algorithm as a function of scatter angle. The minimum near 90° is due to the ambiguity in sequences when the energy deposited at each site is nearly equal.

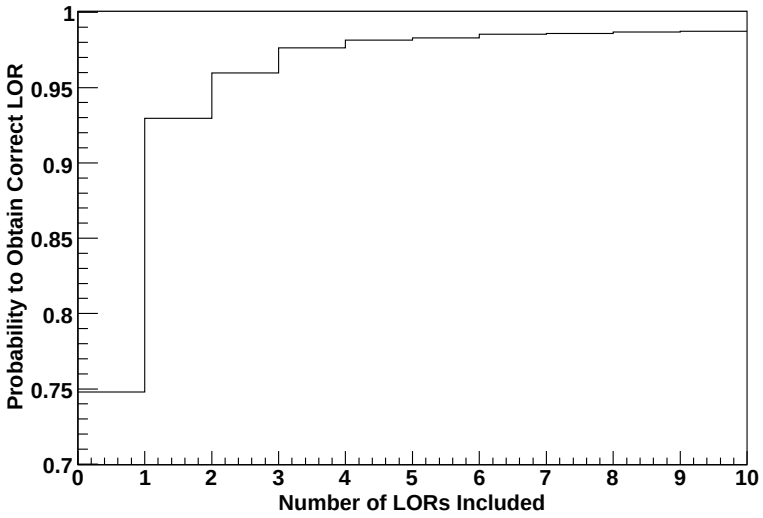

Figure 2.4: The ability of the Compton reconstruction algorithm to find the correct LOR within the ten most probable interaction sequences. The most probable sequence is the correct LOR in less than 75% of the events. The correct sequence is in the top two sequences in over 90% of the events.

comparing it to θ_E the sequence can be tested to determine if it is feasible or not. The TPC returns the energetics and positions of the interactions providing the ability to perform this test. The energies and positions measured by the detector are not perfect, therefore each interaction is given a test score, χ^2, defined as:

$$\chi^2 = \frac{(\cos\theta_E - \cos\theta_G)^2}{(\Delta\cos\theta)^2} \tag{2.3}$$

where $\Delta\cos\theta$ is the uncertainty in the angle due to the position and energy resolution of the system [11]. The χ^2 is calculated at each step in the interaction sequence and summed over all interaction points to give a combined test score. Each conceivable sequence is considered and given a test score. The sequence with the lowest χ^2 is the most likely sequence and the first interaction points are chosen as the correct LOR. There are certain situations where the correct sequence is ambiguous and the most likely LOR is not the correct one. The ability of the Compton reconstruction algorithm to find the correct LOR is shown in Figure 2.2. In the 1–1 topology there are no angles to compare and the sequence is given a χ^2 of zero. For 1–2, 2–2 and 2–3 topologies the Compton reconstruction algorithm performs poorest, only finding the correct LOR close to 50% of the time for the 2–2 topology. This is due to the ambiguity in the correct interaction sequence for a TPC with two interaction points. If the energies deposited in the detector at each interaction point are very close then the scatter angle is close to $\frac{\pi}{2}$. This makes both possible photon paths, from one point to the other, equally likely. Those topologies not equivalent to N–2 or 2–N perform better as there is less ambiguity in the path of the photon. The ability of the Compton reconstruction to identify the correct sequence for the 1–2 topology at various angles is shown in Figure 2.3.

The data set used in this study, as described in § 3.1, contains no photons scattered before entering the LXe. Without any scatter data the performance of the Compton reconstruction algorithm can be tested by comparing the correct LOR to the LOR returned from the algorithm. Although the lowest χ^2 does not always indicate the correct LOR, the correct sequence is one of the sequences

considered by the Compton reconstruction algorithm. The probability that the correct LOR is found within the N most likely sequences, for $N = 1$ to $N = 10$, is shown in Figure 2.4. The most likely topology is the 1–2 topology and the probability that the correct sequence is found for the 1–2 topology is around 75%. This is the dominant effect in Figure 2.4 while only considering the most likely sequences. By considering two sequences the probability that the correct LOR is within that set rises to over 90%. This is due to the ambiguity in those events where there are two interactions in one TPC. By considering two sequences both ambiguous sequences are included. As more sequences are considered the probability that the correct sequence is included falls off exponentially. The difficulty in including these less likely LORs into the image is that too much scatter information could be introduced.

2.2 MLEM

The information obtained from the Compton reconstruction algorithm confines the location of the decay event to a line across the object. To get a tomographic image of the object a reconstruction technique is used. Various strategies exist for reconstructing PET images. A method must be chosen which can preserve the high spatial resolution information obtained by the LXePET detector. One of these reconstruction techniques is the list mode maximum likelihood estimation maximization (MLEM) algorithm. As compared to other reconstruction methods list mode MLEM provides improved spatial resolution, however it is much more computationally intensive [13]. The MLEM algorithm is an iterative optimization method which maximizes the likelihood function. An initial guess at the image solution is made and compared to the data. The likelihood is a statistical measure of the difference between the measured and estimated image solution. The image converges when the difference is minimized. The intensity estimate in each voxel

j for iteration $n+1$ depends on the previous iteration n:

$$f_j^{n+1} = \frac{f_j^n}{s_j} \frac{\sum_i p_{ji}}{\sum_k p_{ik} f_k^n} \tag{2.4}$$

where s_j is the sensitivity value for voxel j and p_{ij} is the probability that a photon emitted from pixel i will be detected in pixel j. If the estimated solution eactly equals the measured data then $f_j^{n+1} = f_j^n$ and this is very unlikely. The MLEM algorithm is performed a certain number of iterations or until convergence to a certain level.

The LORs assigned by the Compton reconstruction algorithm are not always the correct LORs for a given event. The χ^2 value is related to the probability that an assigned LOR is the correct one. If a statistical probability is assigned to a LOR there are two ways this information can be added into the image. The LOR can be multiplied in the input data set or the p_{ij} can be altered to incorporate the probability that the LOR is correct. External weighting schemes multiply the LOR before applying the MLEM algorithm, while internal schemes weight p_{ij}. Internal weighting MLEM methods have been developed for CT imaging [12].

Chapter 3

Experimental Methods

The data used for this study were obtained from simulation. Simulated data provides the ability to compare the correct interaction sequences to those found from the Compton reconstruction algorithm and characterize its performance. The simulation is outlined in § 3.1, image reconstruction is described in § 3.2 and the analysis techniques are defined in § 3.3.

3.1 Geant4 Simulation

A simulation of a liquid xenon PET (LXePET) system has been developed [11]. This was accomplished using the Geant4 simulation package [8]. The detector was simulated using a ring of twelve trapezoidal time projection chambers (TPCs) in the liquid Xe space (a diagram of the detector showing decay events is shown in Figure 3.1). This space is contained in a stainless steel vessel that is thermally insulated by a vacuum space. Each TPC has two arrays of large area avalanche photodiodes (LAAPDs). The LAAPDs were not simulated directly, but were parametrized and applied to the data. The cathode is 10 cm by 3.2 cm and is located 11 cm from the anode with dimensions 10 cm by 9.2 cm. For this study ^{18}F was chosen as the positron source. Upon decay the energy of the positrons was sampled from a continuous distribution. The positrons were then tracked until annihilation where two photons were produced. The photons can interact with the phantom (the different phantoms used are described in § 3.3.1) and all the components of the detector. The photons get tracked into the LXe where the energy and 3D position of the photon interaction is recorded. The response of

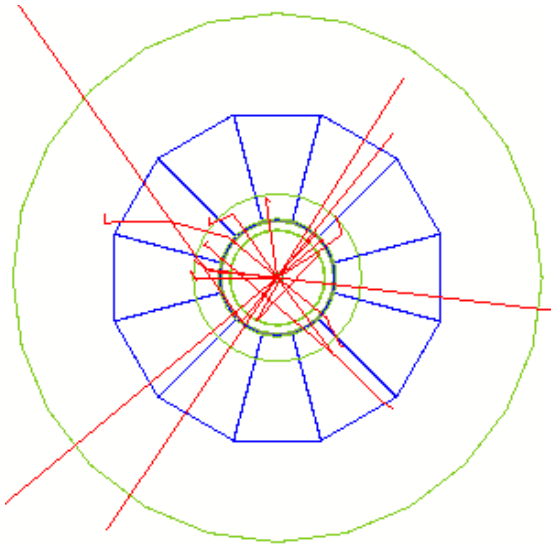

Figure 3.1: Axial view of the simulated detector geometry showing decay events. The TPCs are outlined in blue, the vessel housing the LXe and the TPCs is outlined in green and the red lines show the photon paths. Some photons do not get captured by the detector while some photons scatter before entering the liquid Xe.

the detector was simulated, which applies blurring to the position reconstruction and energy reconstruction. The number of scintillation photons and ionization charges was simulated and only those events with combined energy 450–600 keV were accepted. The first interaction points are then found using the Compton reconstruction algorithm outlined in § 2.1. The resulting LOR is recorded in the list mode format. Only those LORs passing through the phantom are included and any photons scattered prior to entering the liquid xenon are rejected. This criteria was chosen to test the ability of the Compton reconstruction algorithm to identify the correct LOR. For the mouse phantom 25 million decay events were simulated resulting in close to two million LORs. To obtain a similar number of LORs for the rat phantom 50 million decay events were simulated.

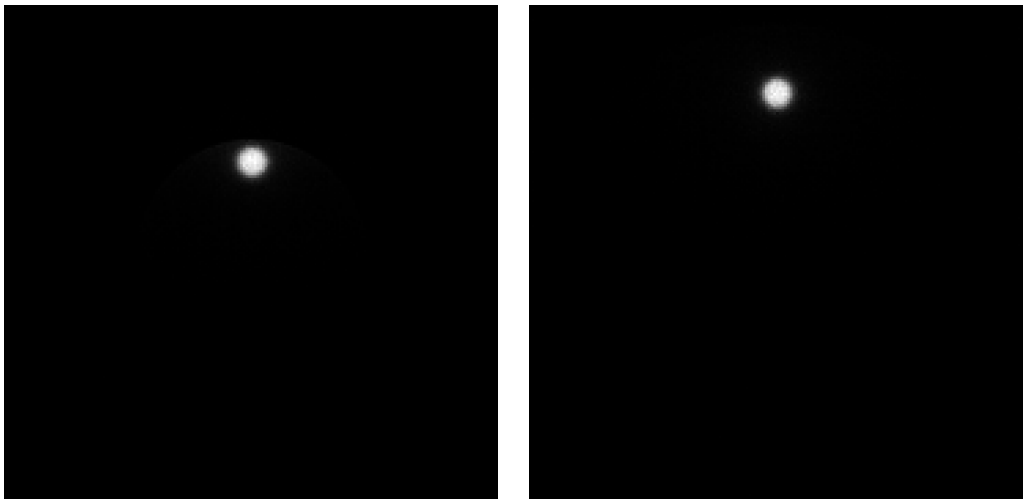

(a) Mouse phantom (b) Rat phantom

Figure 3.2: List mode MLEM reconstructed images for the mouse and rat phantoms. Full 3D images are summed along the axial direction to produce 2D transaxial images. Each image is 180×180 pixels with a pixel size of 0.3 mm. Only LORs passing through the phantom are accepted.

3.2 Image Reconstruction

The simulated data is reconstructed using a list mode MLEM algorithm. Each LOR is represented by one line in the list mode. Each line consists of six values: the three coordinates of the first interaction point for each photon. Full 3D images are 180×180×180 pixels and reconstructed using a voxel size of $(0.3\ \text{mm})^3$. The images are centred at the center of the detector. Each reconstruction is done using 100 MLEM iterations. All images are summed along the axial direction to produce a 2D transaxial image. Reconstructed images are shown in Figure 3.2. The raw images are viewed using the public domain software ImageJ. The only visible feature in the images is the cylindrical source in the phantoms (phantoms are described in § 3.3.1).

3.3 Analysis Tools

Images are degraded when an incorrect LOR is included in image reconstruction. These incorrect LORs can be classified as scattered events. Therefore, the proportion of scattered events included in the image data provides a direct indication of the image quality. The National Electrical Manufacturers Association (NEMA) provides a set of standardized tests for comparing the abilities of PET imaging devices. The tools outlined in this section were developed to adhere to the NEMA protocols.

3.3.1 Phantoms

In the laboratory the most widely used small animals are the mouse and rat. To represent these animals, standardized phantoms are used for testing and charactizing a PET detector. Each phantom is constructed of high-density polyethylene in the shape of a solid right circular cylinder. The mouse phantom has dimensions 70.0 ± 0.5 mm in length by 25.0 ± 0.5 mm in diameter. The larger rat phantom has dimensions 150.0 ± 0.5 mm in length by 50.0 ± 0.5 mm in diameter. Offset radially from the center is a hollow cylinder, parallel to the phantom, with diameter 3.2 mm. The offset is 10.0 mm in the mouse phantom and 17.5 mm in the rat phantom. The hollow cylinder is filled with a radioactive source to produce a source 3.2 mm in diameter. The phantoms provide a convenient way to test the response of a PET detector to a source distribution and measure the amount of scattered events entering into the image data.

3.3.2 Scatter Fraction Calculation

One measure of the system's sensitivity to scattered radiation is the scatter fraction (SF). This is defined as the ratio of the scattered events to the sum of the scattered and true events. The scatter fraction is determined following the NEMA standard [1]. The data are first arranged into 2D projection space representations

(sinograms) with one dimension the radial distance from the detector center and the second dimension the projection angle. Using the dimensions of the phantom any signal in the sinogram farther than 8 mm from its edges is set to zero. At each projection angle in the sinogram the center of the positron source is found. The center is found by determining the position with the highest signal. All positions for a given angle are then shifted to place the center at zero. The sinogram is then summed along the projection angle to produce a 1D profile. The average values of the sum projection at +7 mm and −7 mm is multiplied by the number of pixels within this region. This estimates the background scatters in the signal region. The background value is added to the sum of the values outside the central 14 mm strip to produce the total number of scattered events, C_s. The total sum of all values in the sum projection is then found to give the total number of events, C_{TOT}. The SF is calculated by

$$\mathrm{SF} = \frac{C_s}{C_{TOT}} \tag{3.1}$$

Typical values for the SF of the mouse and rat phantoms are 8% and 12% respectively. Only true events were considered, therefore the SF is primarily a measure of the Compton reconstruction's inability to determine the correct interaction sequence. When the incorrect sequence is taken as the correct one a LOR passing outside of the phantom can be included in the data. If these LORs have less influence in the data the SF decreases, the line source is more confined to it's actual size and image quality increases.

3.3.3 Image Resolution

The resolution of a detector is characterized by the ability of the system to distinguish between two points after image reconstruction. The standard way to determine the detector's resolution is by comparing the widths of point sources separated by various distances [1]. The width of a point source is defined by its full width at half–maximum amplitude (FWHM) and full width at tenth–

Phantom	FWHM (mm)	FWTM (mm)
Mouse	2.79	5.15
Rat	2.76	5.19

Table 3.1: FWHM and FWTM for the mouse and rat phantoms.

maximum amplitude (FTWM) as shown in Figure 3.3. The point source profile is measured by projecting the image into three one–dimensional profiles in three orthogonal directions. The full source profile is obtained by summing all profiles along a given direction. The FWHM and FWTM are then measured on the sum projected profiles. The profiles are not smooth functions, hence linear interpolation is used between adjacent pixels at half and one–tenth the maximum value. The proposed resolution for the LXePET detector is in the sub–millimeter range.

The FWHM and FWTM are used for characterizing the width of sources in an attempt to represent the amount of scatter extending beyond the source position in each phantom. The radioactive source distribution has a diameter of 3.2 mm. The positron range and photon non–collinearity introduces signal beyond 3.2 mm. The detector's response also causes a widening of the source signal. The image slices in the axial direction are first summed to produce a collapsed two–dimensional image. The profile is then obtained by projecting the image onto the x–axis. The FWHM and FWTM are calculated using the following algorithm: first the maximum value in the profile is determined. Those pixels neighbouring the half or one–tenth maximum value are found to either side of the profile peak value. Linear interpolation finds the position of the FWHM and FWTM to two decimal places in pixel units and is converted to a distance in millimeters using the pixel size. Values for the mouse and rat phantoms are shown in Table 3.1. Profiles are obtained using the tools provided with ImageJ. A profile for the mouse phantom is shown in Figure 3.3. The profiles are normalized so that the area under each profile sums to 1.0.

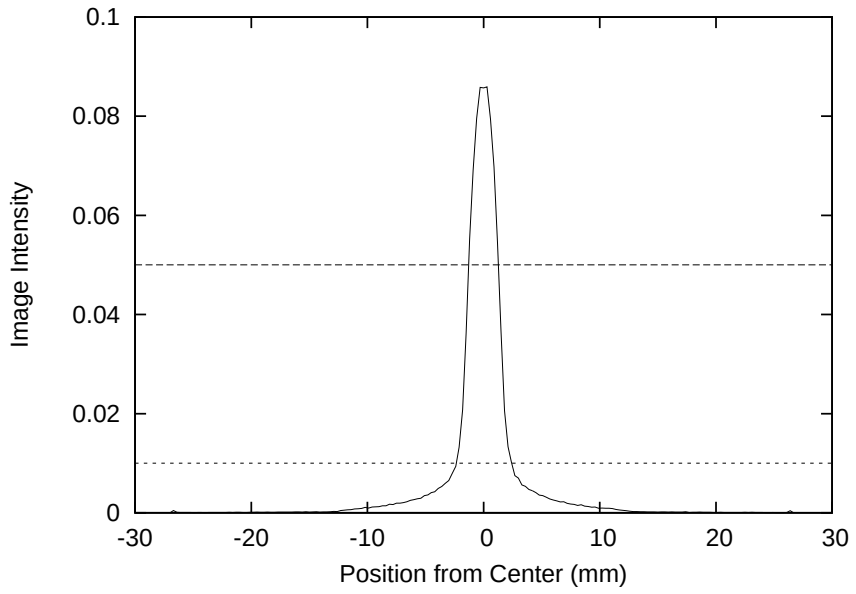

Figure 3.3: Transaxial profile of the mouse phantom projected onto 1D. The horizontal dashed lines at one half and one tenth the peak value indicate the FWHM and FWTM. This provides a measure of the detector resolution by comparing object widths.

Chapter 4

Results and Discussion

The χ^2 value given from the Compton reconstruction (outlined in § 2.1) is related to the probability of obtaining the correct LOR. The smaller the χ^2 the more likely the LOR contains the correct interaction points. This chapter discusses several methods developed which use the χ^2 information in an attempt to produce higher quality images. There are two classes of weighting scheme developed: internal and external, shown in Figure 4.1. In external schemes the LORs are multiplied in the list mode before image reconstruction. In internal schemes the LORs are weighted inside the reconstruction algorithm. The internal scheme provides two key advantages over the external scheme. The first major advantage is processing time. The MLEM algorithm calculates projections of the dataset and compares it to the estimated image solution [14]. Multiplying the number of lines in the list mode input significantly expands the processing time. The other major advantage is that external weights are integers, whereas internal weights also include rationals. To include higher precision in the weights more LORs need to be included. In external schemes a compromise must be made between precision and processing time, but not so in internal schemes. If an external weighting scheme is found to produce high quality images transforming it into an internal scheme will enhance its performance. An external weighting scheme is analyzed in § 4.1 and an internal scheme is analyzed in § 4.2.

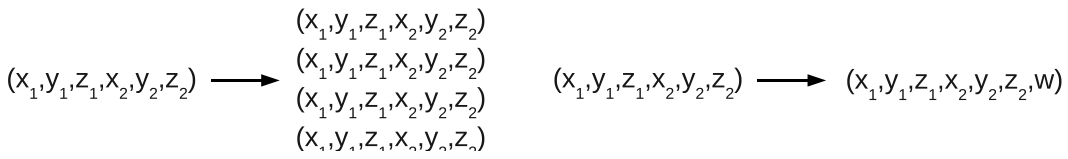

(a) External Scheme (b) Internal Scheme

Figure 4.1: Weighting schemes can be external or internal to MLEM. In the external schemes the LOR is multipled by its weight and added to the list mode data. In the case of Figure 4.1(a) the weight is four. In the internal scheme each LOR is attached a weight that is used in the MLEM image reconstruction. Internal methods produce a smaller set of data as compared to external methods.

4.1 Inverse χ^2 Weighting

The simplest weighting scheme that gives higher weight to higher probability LORs is the inverse χ^2 weighting scheme. The weights, w, are defined as

$$w = \left(\frac{1}{\chi^2}\right)^{\alpha} \tag{4.1}$$

where the exponent α can range from 0–1 for limiting processing time. The LORs with a $\chi^2 > 1$ receive a weight of 1.0 and those LORs from the 1–1 topology receive the maximum weight given to the other topologies. Images produced from this weighting scheme are shown in Figures 4.2 and 4.3 and the associated line profiles are shown in Figure 4.4. Further properties of the reconstructed images are listed in Table 4.1. The scatter fraction present in each reconstructed image decreases as α increases. Furthermore, the FWHM and FWTM decrease to higher α. The inverse χ^2 scheme appears to produce significantly higher quality images. If the maximum weight is much higher than all other weights, the scheme essentially produces an image composed of mainly 1–1 topology events. The proportion of events that are 1–1 topolopy is around 15%. At higher values of α this weighting scheme only uses $\sim 15\%$ of the information gathered by the detector. The sensitivity of a detector is a measure of its efficiency in detecting true events. In the NEMA standard the absolute sensitivity is defined as the fraction

Phantom	α	FWHM (mm)	FWTM (mm)	SF	# LORs
Mouse	0.0	2.79	5.15	0.088	2063534
Mouse	0.1	2.73	4.52	0.024	6199268
Mouse	0.2	2.69	4.18	0.019	43308981
Rat	0.0	2.76	5.19	0.124	1705562
Rat	0.1	2.68	4.48	0.067	6021201
Rat	0.2	2.65	4.19	0.033	61617465

Table 4.1: Properties of reconstructed images for the mouse and rat phantoms using the inverse χ^2 weighting scheme. The resolution of the image increases and the SF decreases to higher exponent α, however the data set grows vastly and requires much more time to process.

of positron–electron annihilation events detected as true coincidence events. The production of annihilation events is a Poisson process. The uncertainty in the number of true LORs is $\approx \sqrt{N}$ and the relative uncertainty is $\approx \frac{\sqrt{N}}{N} = \frac{1}{\sqrt{N}}$. As the number of events is reduced the relative error increases. By only considering 15% of the events the relative uncertainty increases and the sensitivity of the detector is reduced.

Each topology contributes a certain fraction of scattered events to the image. Some of these scattered events are due to Compton scattering outside of the TPC modules, while some of these scattered events are due to improper classification by the Compton reconstruction algorithm. In the 1–1 topology there is only one possible interaction sequence, therefore the correct sequence is always found. These events have a low scatter fraction. This causes the scatter fraction to be weighted by the 1–1 topology scatter events, producing the results in Table 4.1. In the 1–2 topology there can be as much as 50% ambiguity in the correct LOR. This occurs if the energy deposited at each interaction point is almost equal and the scattering angle is the same for each conceivable LOR. This is demonstrated

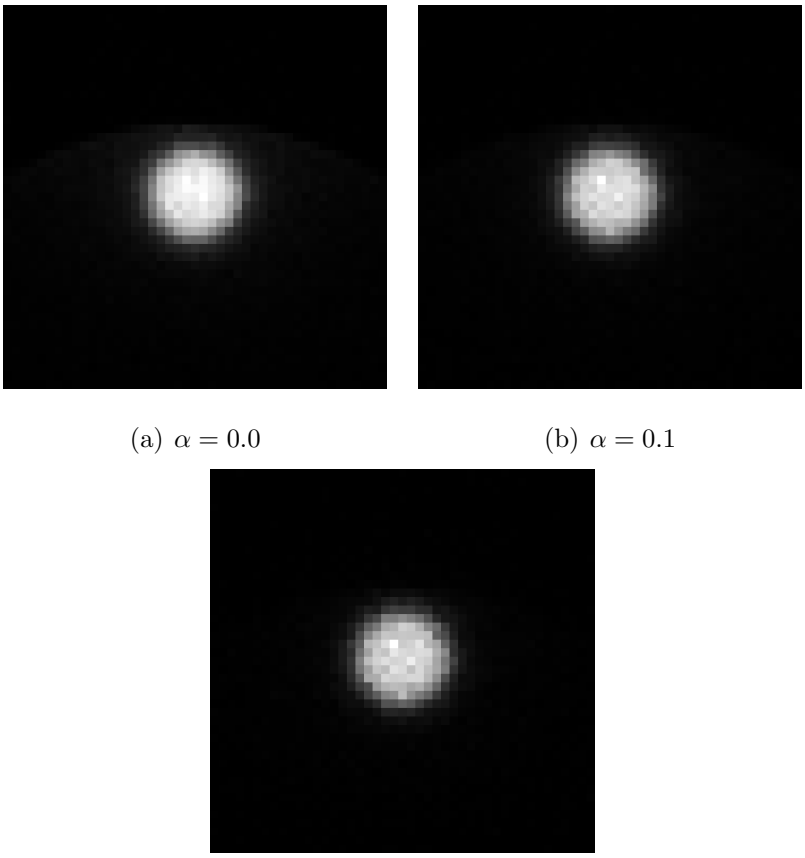

(a) $\alpha = 0.0$ (b) $\alpha = 0.1$

(c) $\alpha = 0.2$

Figure 4.2: MLEM reconstructed images of the mouse phantom for inverse χ^2 weighting exponents of $\alpha = 0.0$ to $\alpha = 0.2$. The amount of scatter decreases in higher weight exponents and the width of the source decreases. Increasing the exponent causes the 1–1 topology events to dominate. This decreases the image sensitivity as only 15% of the events are 1–1 topology.

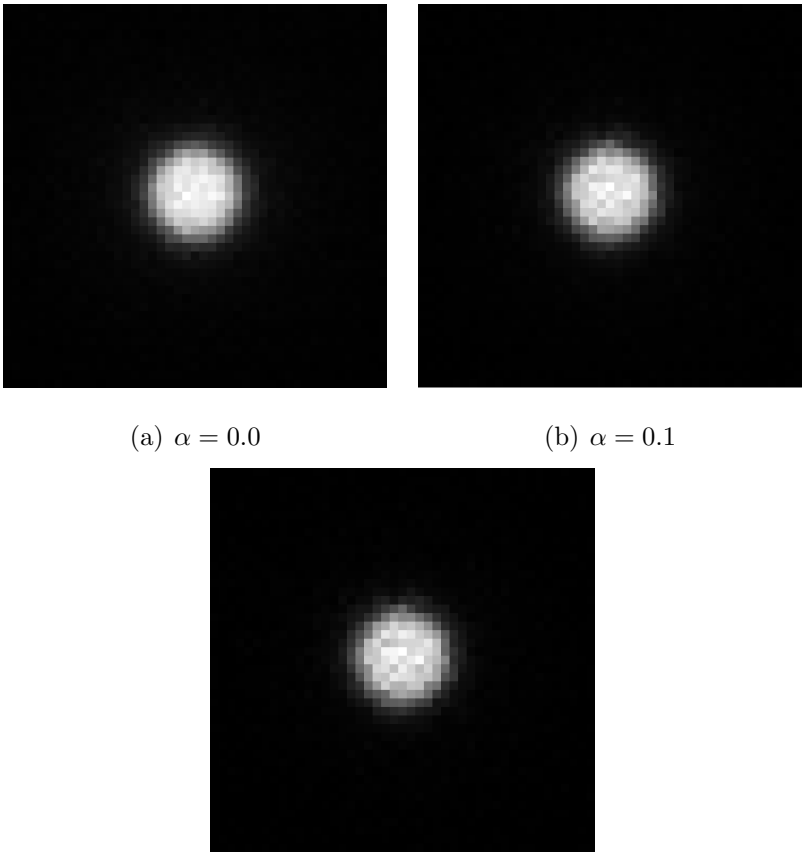

(a) $\alpha = 0.0$ (b) $\alpha = 0.1$

(c) $\alpha = 0.2$

Figure 4.3: MLEM reconstructed images of the rat phantom for inverse χ^2 weighting exponents of $\alpha = 0.0$ to $\alpha = 0.2$. Results are similar to those of the mouse phantom.

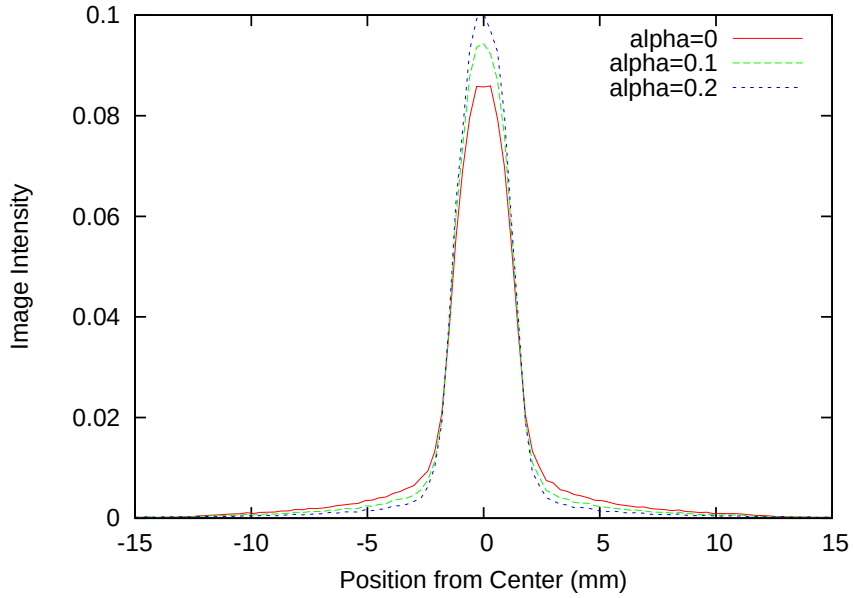

(a) Mouse Profiles

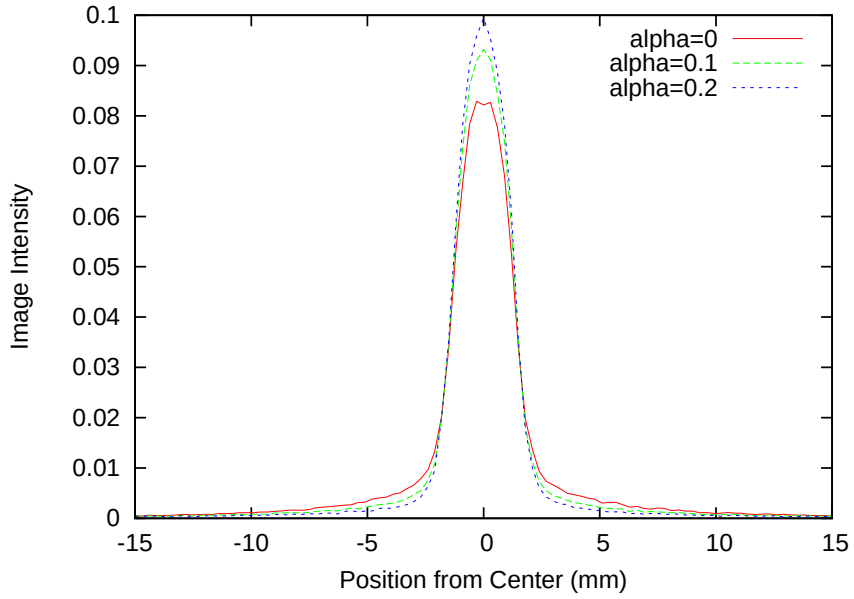

(b) Rat Profiles

Figure 4.4: Profiles of the mouse and rat phantoms for the inverse χ^2 weighting scheme with $\alpha = 0.0$ to $\alpha = 0.2$. The FWHM and FWTM of the source decreases as α increases indicating the amount of scattered signal included in the image is decreasing.

in the poor ability of the Compton reconstruction algorithm for the 1–2 topology. This effect is even greater for the 2–2 topology. At higher topologies the Compton reconstruction algorithm performs better as there are more interaction points. With more interaction points there is less ambiguity in the interaction sequence due to the energetics of Compton scattering as outlined in § 2.1. Images reconstructed using only 1–1 to 1–3 topology Compton reconstructed interaction points are shown in Figures 4.5 & 4.6. The properties of these images are listed in Table 4.2. The poorest reconstructed images are those composed of only 2–2 topology events as they contain the highest proportion of scattered events. The line profiles of the mouse and rat phantoms for each topology are shown in Figure 4.7. The width of the source is the narrowest in the 1–1 topology, while the widest source is reconstructed from 2–2 data. If the Compton reconstruction algorithm is able to better classify the correct LOR for 2–2 topology the reconstructed images will be greatly enhanced. The only parameters which are available from the TPC are position and energy. Any attempt at improving the Compton reconstruction algorithm for these events will have to be able to use these parameters in distinguishing the correct from incorrect interaction sequence.

4.2 Internal MLEM Weighting

A weighting scheme internal to MLEM has the advantage that it reduces the number of LORs included in the list mode file as compared to an internal weighting scheme. The weights can also be given higher precision. In the external schemes a weight gets converted into an integer number of LORs in the list mode and therefore the weight gets truncated. By attaching the weight as an input parameter to the list mode the truncation is not as severe. The Compton reconstruction is not always successful in determining the correct LOR, however the correct interaction sequence is present in the set of sequences considered. By considering only the two most probable sequences the correct LOR is found within

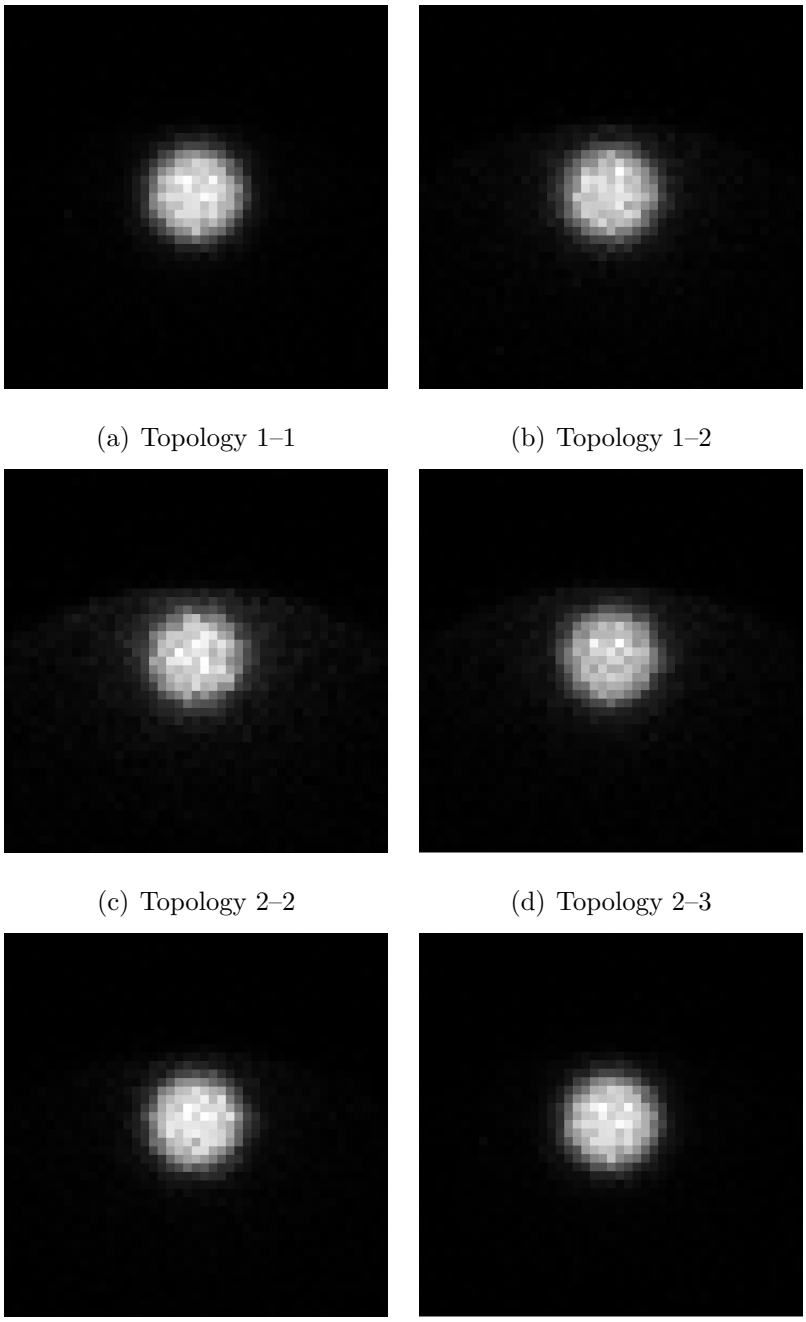

(a) Topology 1–1

(b) Topology 1–2

(c) Topology 2–2

(d) Topology 2–3

(e) Topology 1–3

(f) Correct Sequences

Figure 4.5: MLEM reconstructed images of mouse phantom for topologies 1–1 to 1–3 using Compton reconstructed data. The image using the correct interaction sequences is shown for comparison in Figure 4.5(f). The 2–2 and 2–3 images show the most scatter due to the ambiguity in the LOR for TPCs with two interaction points. The 1–1, 1–2 and 1–3 show the least scatter.

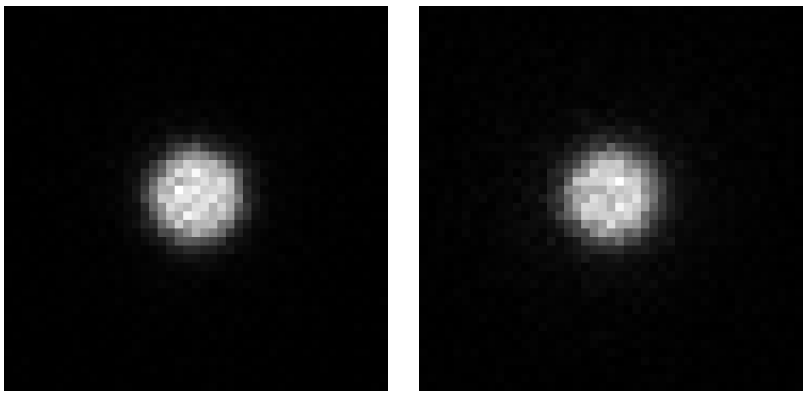

(a) Topology 1–1

(b) Topology 1–2

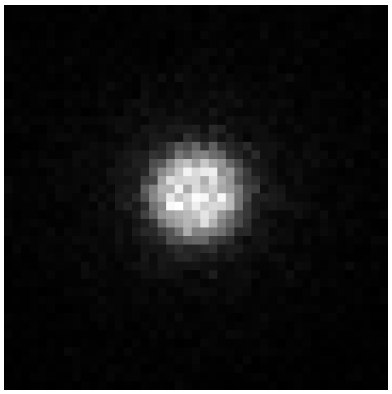

(c) Topology 2–2

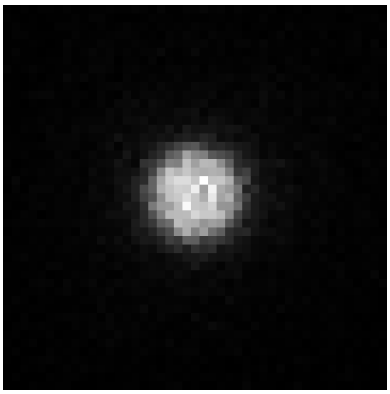

(d) Topology 2–3

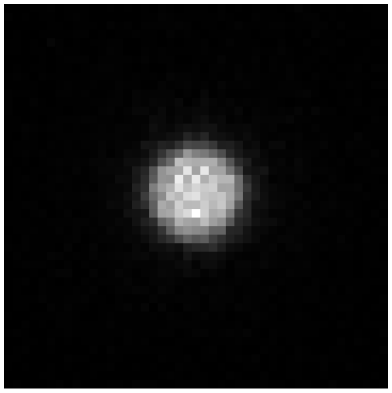

(e) Topology 1–3

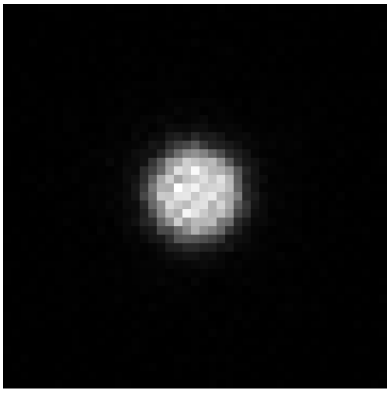

(f) Correct Sequences

Figure 4.6: MLEM reconstructed images of rat phantom for topologies 1–1 to 1–3 using Compton reconstructed data. The image using the correct interaction sequences is shown for comparison in Figure 4.6(f). The worst quality image is from the 2–2 topology, similar to the results from the mouse phantom.

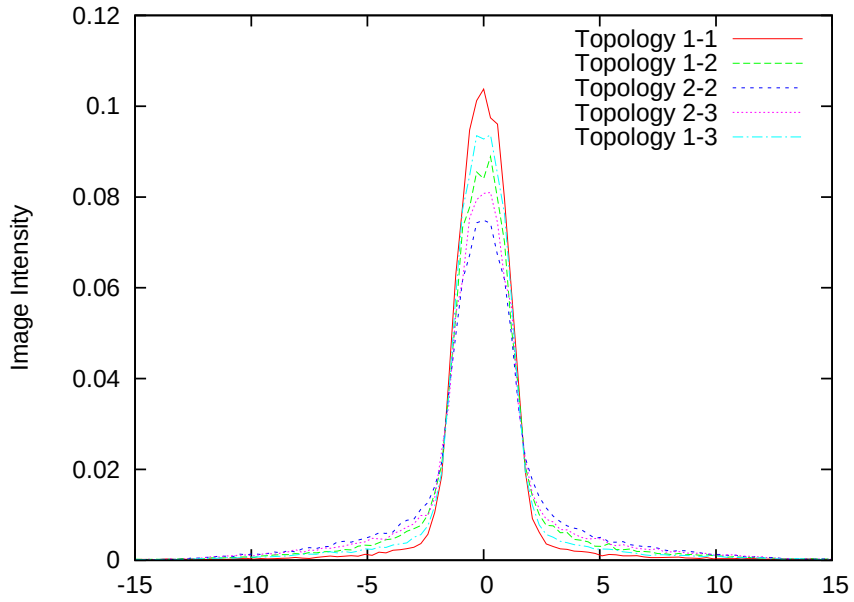

(a) Mouse Profiles

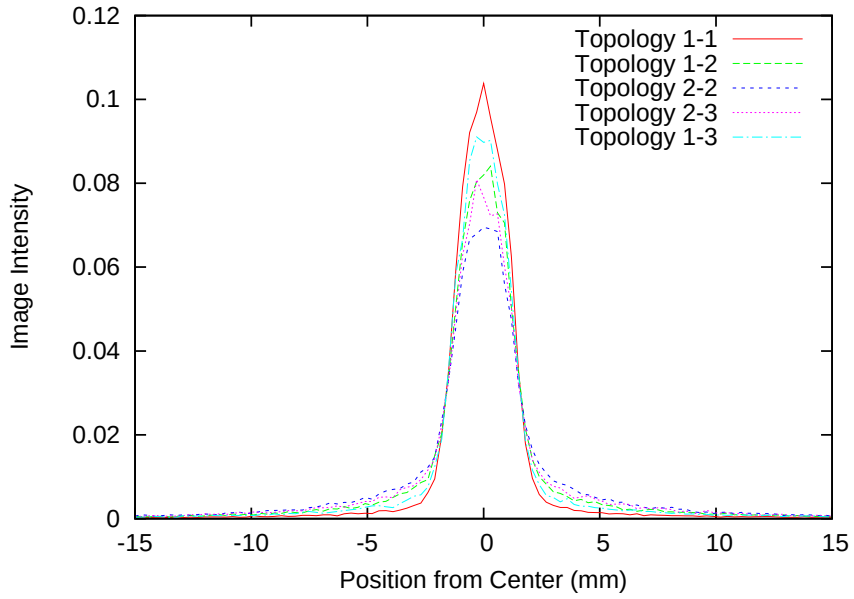

(b) Rat Profiles

Figure 4.7: Profiles of the mouse and rat phantom for each topology. The width of the profile is widest for the 2–2 topology and narrowest for the 1–1 topology.

Phantom	Topology	FWHM (mm)	FWTM (mm)	SF
Mouse	1–1	2.66	4.18	0.019
Mouse	1–2	2.72	5.09	0.084
Mouse	2–2	2.92	7.32	0.142
Mouse	2–3	2.82	6.04	0.125
Mouse	1–3	2.71	4.58	0.064
Rat	1–1	2.61	4.15	0.029
Rat	1–2	2.72	5.43	0.122
Rat	2–2	2.92	7.83	0.198
Rat	2–3	2.72	5.85	0.170
Rat	1–3	2.71	4.62	0.091

Table 4.2: Properties of the mouse and rat phantom images reconstructed for each topology. The 2–2 topology has the worst quality with the largest FWHM and highest SF. All images are reconstructed with the same amount of list mode data.

that set over 90% of the time. By considering the five most likely sequences the probability rises to 98%. A scheme which includes the information from all the true LORs while limiting the amount of scatter information being introduced into the image can potentially produce higher quality images. To attempt this the following weighting scheme was implemented:

$$w_i = 1 - \frac{\chi_i^2}{(n-1)\sum_j^N \chi_j^2} \tag{4.2}$$

where the index i represents the i^{th} most probable sequence and n is a normalization factor. The normalization factor ensures that each event provides a total weight of 1.0 to the MLEM reconstruction. The index j runs from 0 (corresponding to the lowest χ^2 sequence) to the total number of desired sequences, N, included. If the total number of possible sequences, m, for a given topology is

Phantom	# Sequences Considered	FWHM (mm)	FWTM (mm)	# LORs
Mouse	1	2.78	5.14	2063534
Mouse	2	2.80	5.34	3813775
Mouse	3	2.84	6.16	4885175
Mouse	4	2.87	7.09	5956575
Mouse	5	2.89	7.48	6659060
Rat	1	2.76	5.19	1705562
Rat	2	2.78	5.43	3144414
Rat	3	2.81	6.30	4016562
Rat	4	2.84	7.10	4888710
Rat	5	2.86	7.47	5459897

Table 4.3: Properties of the mouse and rat images reconstructed with the internal MLEM weighting scheme. By including the two most likely LORs the image quality is not improved. As more LORs are included the image quality worsens, furthermore the size of the data set increases and takes longer to process.

less than N all w_i for i larger than m are given a weight of zero. The results of the internal weighting scheme are shown in Figures 4.8 & 4.9 and Tables 4.3. The profiles of the mouse and rat phantoms for including the 1 to 5 most likely LORs are shown in Figure 4.10. As more sequences are considered in the weighting scheme the FWHM and FWTM increases. This indicates that the amount of scatter in the image is also increasing and that no significant increase in image quality is obtained with this weighting scheme. As more LORs are considered the amount of scatter information included in the image dominates the true LOR information. A scheme which further reduces the weight to the ambiguous LORs could remove the prevalance of the incorrect LORs and increase image quality.

An external scheme adopting a similar normalized weight produces the results shown in Figure 4.11. The weights are calculated according to Equation 4.2

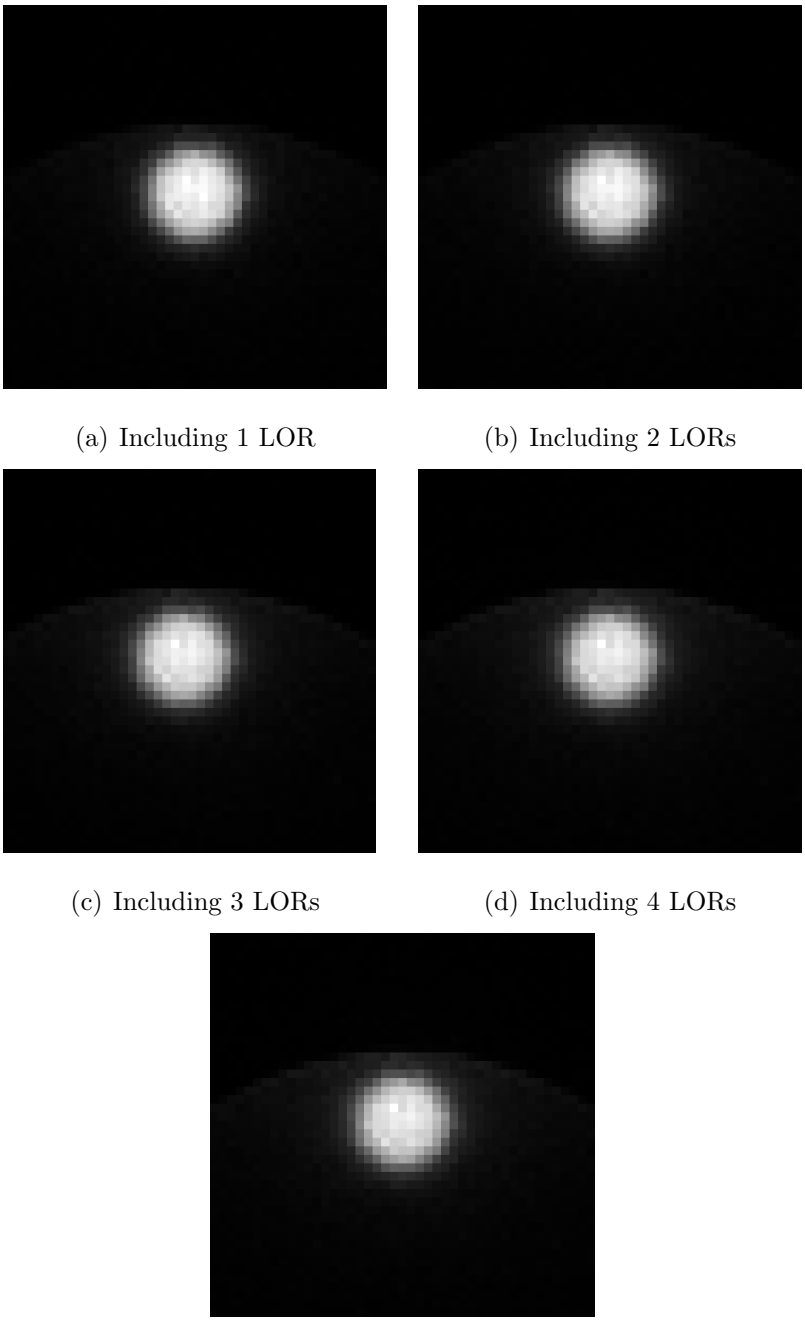

(a) Including 1 LOR

(b) Including 2 LORs

(c) Including 3 LORs

(d) Including 4 LORs

(e) Including 5 LORs

Figure 4.8: MLEM reconstructed images of mouse phantom for the internal weighting scheme. As more sequences are included in the weighting scheme more scatter information is used without including a significant amount of true LOR information. There is no signifcant increase in image quality from Figure 4.8(a) to Figure 4.8(b). Image quality worsens in Figures 4.8(c)–4.8(e).

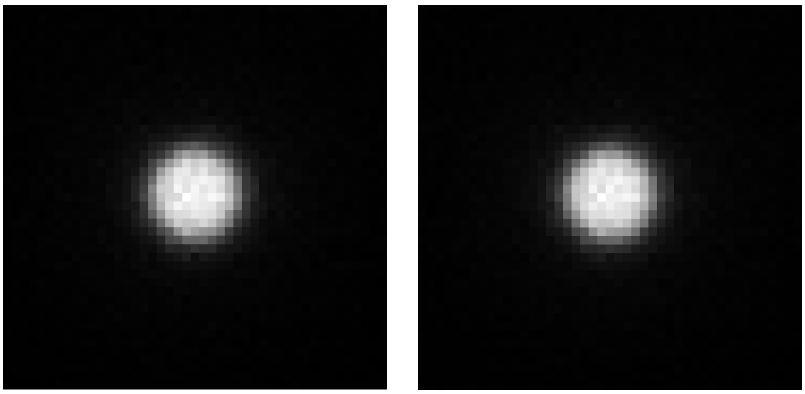

(a) Including 1 LOR

(b) Including 2 LORs

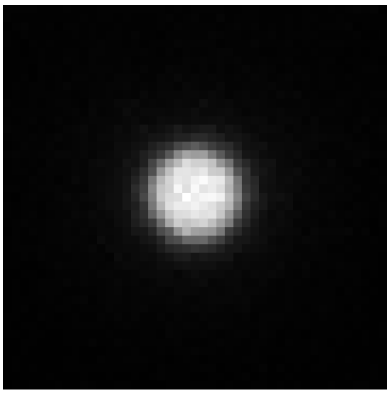

(c) Including 3 LORs

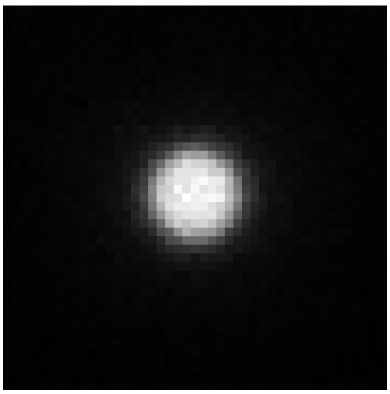

(d) Including 4 LORs

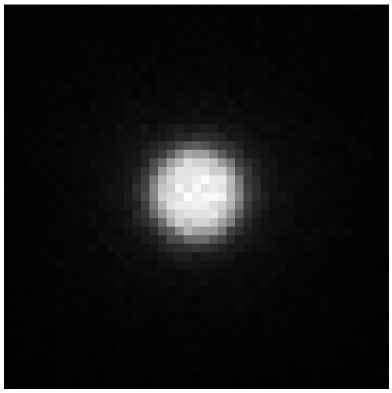

(e) Including 5 LORs

Figure 4.9: MLEM reconstructed images of rat phantom for the internal weighting scheme. No significant increases in image quality are made by including more than the first LOR. The results are similar to the mouse phantom.

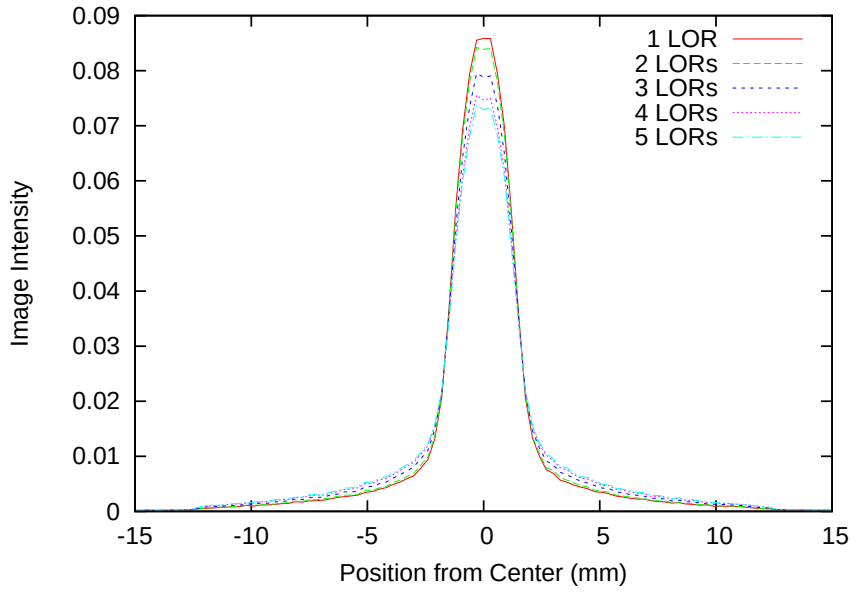

(a) Mouse profiles

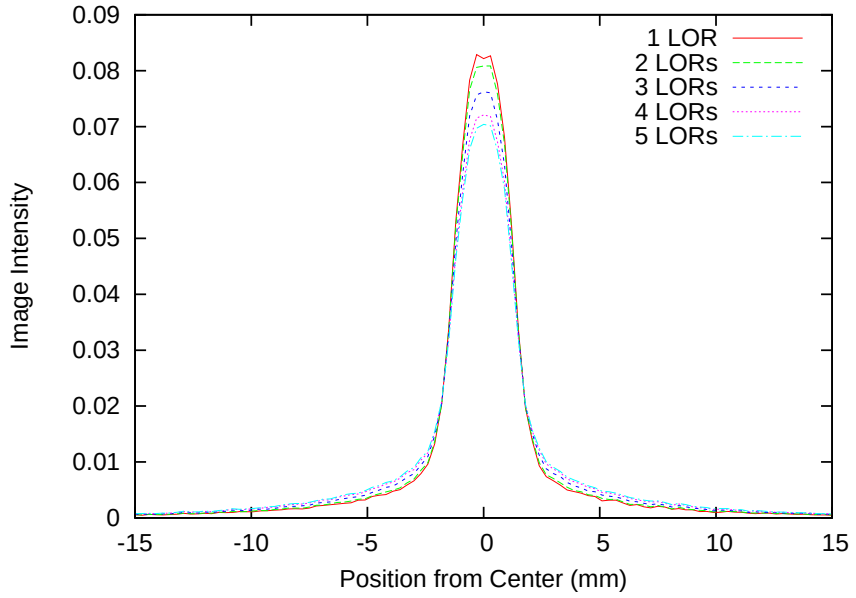

(b) Rat profiles

Figure 4.10: Profiles of the mouse and rat phantoms for the internal weighting scheme. The lowest FWHM and FWTM occur when only the most likely LOR is considered.

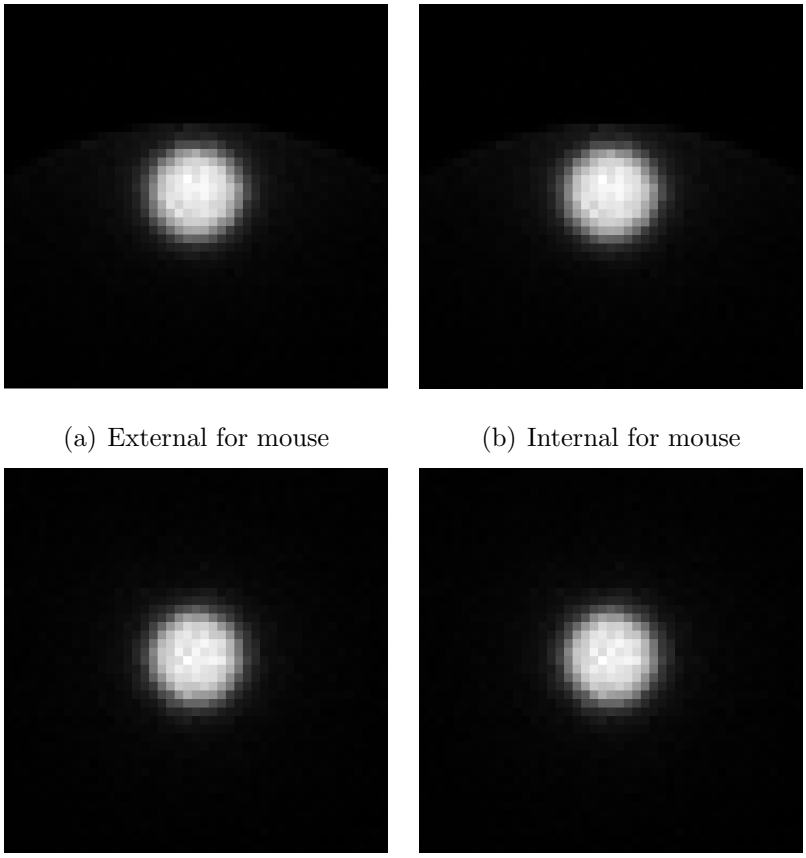

(a) External for mouse (b) Internal for mouse

(c) External for rat (d) Internal for rat

Figure 4.11: MLEM reconstructed images of the mouse and rat phantoms for an external weighting scheme similar to Equation 4.2. Only the top two LORs are considered when assigning weights. The corresponding internal weighting scheme images are also shown for comparison. The images produced from the internal scheme are similar to those produced from the external scheme.

and converted to an integer on the range [0 : 10]. The weight is essentially rounded to the first decimal place and multiplied by ten. The profiles of the internal as compared to the external scheme show no significant decrease in source width indicating that the methods are similar. An external method can be easily transformed into an internal method.

Chapter 5

Conclusion

Simulation of the high resolution LXePET detector provides an important testing ground to develop new techniques for enhancing the system's performance. A framework has been established for testing the performance of the high resolution LXePET detector. Simulations of the full LXePET detector were carried out in order to characterize various weighting schemes. The weighting schemes investigated were applied externally and internally to the MLEM image reconstruction method. The external methods create large datasets which take a large amount of time to process. The list mode iterative MLEM algorithm is more computationally intensive than other reconstruction methods and adding an external weighting scheme further increases the time to reconstruct images. The transformation of an external to an internal scheme using MLEM image reconstruction is simple and introduces no significant increase in processing time.

The external and internal weighting schemes defined and investigated did not provide a significant increase in image quality without compromising image sensitivity. The abilities of the Compton reconstruction algorithm have shown that the ambiguity in the 1–2, 2–2 and 2–3 sequences is the main contributor to the scatter fraction in the image. An improvement in the Compton reconstruction algorithm to correctly determine the correct sequence for these ambiguous events will prove to greatly improve image quality. The only information the detector obtains about these events is in the form of the 3D interaction point positions and the deposited energy. Therefore, any improvement in determining the correct sequences will have to use the interaction point positions and deposited energy in a new way to separate out the correct from incorrect sequences.

In conclusion, Compton weighting schemes have shown potential in creating high quality images in PET. External methods are cumbersome and require an unnecessary amount of time to reconstruct images. Internal methods provide no extra time for reconstructing images and perform better than any external scheme. Further analysis on the performance of the detector will have to be completed to determine the best way to assign weights to each LOR.

Bibliography

[1] *NEMA Standards Publication NU4-2008: Performance Measurements of Small Animal Positron Emission Tomographs*. National Electrical Manufacturers Association, Rosslyn, VA, 2008, 2008.

[2] Adam Alessio, Erik Butterworth, James Caldwell, and James Bassingthwaighte. Quantitative imaging of coronary blood flow. *Nano Reviews*, 1(0), 2010.

[3] E. Aprile, A. E Bolotnikov, A. I. Bolozdynya, and T. Doke. *Noble Gas Detectors*. Wiley-VCH Verlag GmbH & Co, KGaA, Weinheim, 2006.

[4] E. Aprile and T. Doke. Liquid xenon detectors for particle physics and astrophysics. *Reviews of Modern Physics*, 82:2053–2097, July 2010.

[5] V. M. Atrazhev, A. V. Berezhnov, D. O. Dunikov, I. V. Chernysheva, V. V. Dmitrenko, and G. Kapralova. Electron transport coefficients in liquid xenon. In *IEEE International Conference on Dielectric Liquids*, pages 329–332, 2006.

[6] S. E. Boggs and P. Jean. Event reconstruction in high resolution Compton telescopes. *Astronomy and Astrophysics Supplement Series*, 145:311–321, August 2000.

[7] C. M. Clements. Simulations of a high–resolution micro–pet system based on liquid xenon. Master's thesis, UBC, Canada, 2011.

[8] Geant4 Collaboration. Geant4-a simulation toolkit. *Nuclear Instruments and Methods in Physics Research A*, 506:250–303, July 2003.

[9] J. L. Humm, A. Rosenfeld, and A. Del Guerra. From pet detectors to pet scanners. *European Journal of Nuclear Medicine and Molecular Imaging*, 30:1574–1597, 2003.

[10] T. K. Lewellen. TOPICAL REVIEW: Recent developments in PET detector technology. *Physics in Medicine and Biology*, 53:287, September 2008.

[11] A. Miceli, J. Glister, A. Andreyev, D. Bryman, L. Kurchaninov, P. Lu, A. Muennich, F. Retiere, and V. Sossi. Simulations of a micro-PET system based on liquid xenon. *Physics in Medicine and Biology*, 57:1685–1700, March 2012.

[12] M. Oehler and T. M. Buzug. Modified MLEM Algorithm for Artifact Suppression in CT. In *IEEE Nuclear Science Symposium Conference Record*, pages 2511–3518, 2006.

[13] M. E. Phelps. *Physics, Instrumentation, and Scanners*. Springer Science, New York, NY, USA, 2006.

[14] G. B. Saha. *Basics of PET Imaging: Physics, Chemistry, and Regulations*. Springer Science, New York, NY, USA, 2010.